J. Fluid Mech. (2012), *vol.* 703, *pp.* 255–278.
doi:10.1017/jfm.2012.212

Flow topology in compressible turbulent boundary layer

Li Wang and Xi-Yun Lu†

Department of Modern Mechanics, University of Science and Technology of China, Hefei, Anhui 230026, China

(Received 26 June 2011; revised 25 April 2012; accepted 29 April 2012; first published online 14 June 2012)

The flow topologies of compressible turbulent boundary layers at Mach 2 are investigated by means of direct numerical simulation (DNS) of the compressible Navier–Stokes equations, and statistical analysis of the invariants of the velocity gradient tensor. We identify a preference for an unstable focus/compressing topology in the inner layer and an unstable node/saddle/saddle (UN/S/S) topology in the outer layer. The dissipation and dissipation production originate mainly from this UN/S/S topology. The enstrophy depends mainly on an unstable focus/stretching (UFS) topology, and the enstrophy production relies on a UN/S/S topology in the inner layer and on a UFS topology in the outer layer. The compressibility effect on the statistical properties of the topologies is investigated in terms of the 'incompressible', compressed and expanding regions. It is found that the locally compressed region tends to be more stable and the locally expanding region tends to be more dissipative. The compressibility is mainly related to unstable focus/compressing and stable focus/stretching topologies. Moreover, the features of the average dissipation, enstrophy, dissipation production and enstrophy production of the various topologies are clarified in the locally compressed and expanding regions.

Key words: compressible boundary layers, turbulent boundary layers

1. Introduction

Owing to the obvious importance of fundamental research in turbulence, great effort has been made to study the local flow topology in turbulent flows. The topological methodology is based on an analysis of the velocity gradient tensor invariants and utilizes critical point theory to classify the local flow topologies (Perry & Chong 1987; Chong, Perry & Cantwell 1990). Usually, the tensorial invariants are essential for understanding the kinematics and dynamics of turbulent motions (Wallace 2009). For example, the tensorial invariants can be used to educe the vortical structures (Soria & Cantwell 1994; Jeong & Hussain 1995; Chacín, Cantwell & Kline 1996; Chong *et al.* 1998; Bermejo-Moreno, Pullin & Horiuti 2009) and to reveal turbulence processes such as dissipation (Andreopoulos & Honkan 2001; Lee, Girimaji & Kerimo 2009), scalar mixing (Abe, Antonia & Kawamura 2009) and vortex stretching (Buxton & Ganapathisubramani 2010). Moreover, the dynamics can be used to model the

† Email address for correspondence: xlu@ustc.edu.cn

subgrid-scale stress tensor (Cantwell 1992; Chertkov, Pumir & Shraiman 1999; van der Bos *et al.* 2002; Wang *et al.* 2006; Li *et al.* 2009) and for analysing the intermittency of turbulence (Li & Meneveau 2005, 2006; Meneveau 2011).

A general classification of flow fields based on the invariants of the velocity gradient tensor was proposed by Chong *et al.* (1990). For incompressible turbulence, as the first invariant (P) is zero, a turbulent flow field can thus be described by the two-dimensional plane of the second (Q) and third (R) invariants. Extensive investigations of the statistical properties in the Q–R plane have been performed numerically and experimentally. Perry & Chong (1994) and Soria *et al.* (1994) analysed the topology of fine-scale motions for time-developing mixing layers and found that motions with large positive values of Q are most likely to have a topology of stable focus/stretching. Blackburn, Mansour & Cantwell (1996) investigated the topological features of the velocity gradient field of turbulent channel flow. The joint probability density functions (p.d.f.s) of R and Q were analysed to indicate that topologies of stable focus/stretching and unstable node/saddle/saddle are the preferred ones away from the wall. Moreover, the topology of turbulent boundary layers was studied using the invariants of the velocity gradient tensor (e.g. Chong *et al.* 1998; Chacin & Cantwell 2000). They revealed that the joint p.d.f.s exhibit a self-similar teardrop shape from the buffer layer onwards. Ooi *et al.* (1999) studied the topology of isotropic turbulence and found that the joint p.d.f.s are similar for various turbulent flows, suggesting a certain universality in the Q–R plane for small-scale motions of turbulence. The existence of the teardrop shape of the joint p.d.f. was also confirmed experimentally in turbulent boundary layers (e.g. Andreopoulos & Honkan 2001; Elsinga & Marusic 2010*a*). Recently, Elsinga & Marusic (2010*b*) provided an explanation for the universal teardrop shape in terms of an evaluation of the average flow pattern in the local coordinate system defined by the eigenvectors of the strain-rate tensor. In addition, Lüthi, Holzner & Tsinober (2009) expanded the Q–R plane to three dimensions by the decomposition of R into its strain production and enstrophy production terms and observed that non-locality plays an important role in the evolution of the velocity gradients.

The statistical properties of turbulence in the Q–R plane are investigated extensively. Nomura & Post (1998) analysed the structure and dynamics of vorticity and strain rate in incompressible homogeneous turbulence by examining the scatter plots of Q and R at different times. Chacin & Cantwell (2000) studied the generation of Reynolds stress, turbulent kinetic energy and dissipation in the Q–R plane. Diamessis & Nomura (2000) and Nomura & Diamessis (2000) utilized conditional sampling on different regions in the Q–R plane to analyse the interaction between strain and vorticity in homogeneous sheared turbulence. Tsinober (2000) qualitatively summarized the local flow properties in the Q–R plane and indicated that the enstrophy production is large in the stable focus/stretching topology and the total dissipation production is large in the unstable focus/compressing topology. Da Silva & Pereira (2008) and Khashehchi *et al.* (2010) dealt with a detailed characterization of the dynamics, geometry and topology of the flow across the turbulent/non-turbulent interface in jets. Gualtieri & Meneveau (2010) studied the joint p.d.f.s of Q and R for isotropic turbulence subjected to a straining and destraining cycle and revealed the features of non-equilibrium turbulence. Bijlard *et al.* (2010) investigated the local flow topology in a particle-laden turbulent channel flow and analysed the effects of the particles on the flow field.

Compared to the extensive research into flow topology in incompressible turbulent flows described above, the relevant study of compressible turbulence is limited. Maekawa, Hiyama & Matsuo (1999) dealt with the scatter plots of the tensorial invariants for decaying isotropic compressible turbulence and observed that topologies

of unstable node/saddle/saddle and stable focal/stretching in the Q–R plane prevail over other topologies for $P > 0$ and $P < 0$. Pirozzoli & Grasso (2004) studied the effect of the initial compressibility on the flow topology in the plane of the second (Q^*) and third (R^*) invariants of the anisotropic part of the velocity gradient tensor for compressible isotropic turbulence. Lee *et al.* (2009) found that the strain-rate statistics strongly depend on the normalized dilatation for decaying compressible turbulence. Suman & Girimaji (2010) investigated the local flow topology in compressible isotropic turbulence and analysed the effects of compressibility on the topology. Moreover, Suman & Girimaji (2009) developed a model for describing velocity gradient dynamics of an isentropic compressible turbulence and confirmed that the joint p.d.f.s of Q and R are closely associated with P. In addition, some investigations into the coherent vortical structures in compressible turbulent boundary layers have been carried out experimentally (e.g. Smith & Smits 1995; Ganapathisubramani, Clemens & Dolling 2006; Elsinga *et al.* 2010) and numerically (e.g. Pirozzoli, Grasso & Gatski 2004; Pirozzoli, Bernardini & Grasso 2008; Ringuette, Wu & Martin 2008; Pirozzoli, Bernardini & Grasso 2010*b*; Wang & Lu 2011). To our knowledge, however, the relevant study of the behaviour of flow topology in compressible turbulent boundary layer has never been performed.

In this paper, the statistical properties of compressible turbulent boundary layers are investigated by means of direct numerical simulation (DNS) at Mach number $Ma = 2.0$ and Reynolds number $Re_\theta = 1350$ based on the momentum thickness. The characteristics of the invariants of the velocity gradient tensor are analysed and the flow topologies are studied. The purpose of this study is to achieve an improved understanding of some of the fundamental topological phenomena in this flow.

This paper is organized as follows. The mathematical formulation, numerical method and computational validation are presented in § 2. The tensorial invariants and local flow topologies are briefly described in § 3. Detailed results are then given in § 4 and concluding remarks in § 5.

2. Computational strategy

2.1. *Mathematical formulation and numerical method*

The statistical properties of compressible turbulent boundary layers are studied by means of DNS. The three-dimensional compressible Navier–Stokes equations are employed. To non-dimensionalize the equations, we use the free-stream variables including the density ρ_∞, temperature T_∞, speed of sound a_∞ and the boundary layer thickness at the inlet δ_0 as characteristic quantities.

The equations are numerically solved by a seventh-order weighted essentially non-oscillatory scheme for the convective terms (Jiang & Shu 1996) and a sixth-order central difference scheme for the viscous terms. The temporal integration is performed using a fourth-order Runge–Kutta algorithm (Shu & Osher 1988). The relevant numerical strategy has been verified to be reliable in the simulation of compressible turbulent boundary layers (e.g. Pirozzoli *et al.* 2004, 2008).

In this study, initial and boundary conditions are presented as follows. The inflow boundary condition for DNS of a turbulent boundary layer is treated using the approach developed by Sandham, Yao & Lawal (2003) and subsequently extended by Li & Coleman (2003) to supersonic flow. The approach has been extensively tested in the literature (e.g. Li & Coleman 2003; Pirozzoli *et al.* 2008; Pirozzoli, Bernardini & Grasso 2010*a*). The velocity profile is obtained from the formulation prescribed by Guarini *et al.* (2000). The temperature profile is initialized using the

Crocco–Busemann integral (White 1974). The velocity disturbances at the inlet are determined and the random velocity fluctuations with a maximum amplitude 4 % of the free-stream velocity are added to the velocity components based on previous studies (Li & Coleman 2003; Pirozzoli *et al.* 2008, 2010*b*). A sponge layer is placed before the outlet boundary where variables are extrapolated from the interior (Adams 1998). No-slip and adiabatic conditions are applied on the wall. In order to minimize the reflection of small disturbances back into the computational domain, non-reflecting boundary conditions are specified at the upper boundary. Periodic conditions are used in the spanwise direction to exploit homogeneity. These mean inflow quantities are imposed as initial conditions throughout the computational domain.

2.2. *Computational overview and validation*

We consider a supersonic turbulent boundary layer with the free-stream Mach number $Ma = 2$ and Reynolds number $Re_{\delta_0} = 13\,500$ based on the free-stream parameters and the boundary layer thickness at the inlet (δ_0). The selected computational parameters are the same as those performed by Pirozzoli *et al.* (2008). The relevant data will thus be employed to validate the present calculation.

The computational domain size and grid resolution have been carefully tested in terms of our extensive grid sensitivity studies. The computational domain is finally chosen as $L_x \times L_y \times L_z = 30\delta_0 \times 6\delta_0 \times 3.7\delta_0$ with the corresponding grid point $1819 \times 331 \times 225$, where x, y and z represent the streamwise, wall-normal and spanwise directions, respectively. The mesh is uniformly distributed in the streamwise and spanwise directions, and the grid is stretched by a hyperbolic tangent mapping function in the wall-normal direction. Wall units are defined in terms of the friction velocity $u_\tau = (\tau_w/\rho_w)^{1/2}$ and the viscous length scale $\delta_v = \nu_w/u_\tau$ evaluated at the wall. In terms of the wall units, the streamwise and spanwise grid spacings are $\Delta x^+ = \Delta z^+ = 4.62$, and the wall-normal grid spacing varies from $\Delta y^+ = 0.9$ at the wall to $\Delta y^+ = 4.1$ at the boundary layer edge with more than 200 grid points within the boundary layer. Moreover, to clearly present the postprocessing, some symbols used in this paper are described as follows. The symbol $\langle\rangle$ means the average in time and in space along the streamwise and spanwise directions. The instantaneous flow field variables are decomposed using either a Reynolds decomposition $f = \bar{f} + f'$, where the overbar represents the average in time and in space along the spanwise direction.

To justify the choice of the spanwise computational domain extent, the two-point correlations of flow variables in the spanwise direction are examined using the definition of Pirozzoli *et al.* (2004). Figure 1 shows typical two-point correlations $R_{\alpha\alpha}(r_z)$ in the spanwise direction or z direction, where α represents the fluctuations of any one of the velocity components u_i (or u, v and w in the x, y and z directions). The correlations decay rapidly, which means that the two-point correlations are sufficiently decorrelated over the spanwise extent. Thus it ensures that the spanwise computational domain is sufficiently wide not to inhibit the turbulence dynamics.

To validate the present simulation, we compare the calculated results with previous data in terms of the mean velocity, Reynolds stress and root-mean-square (r.m.s.) vorticity components. The distribution of the van Driest transformed mean streamwise velocity is shown in figure 2(*a*). It is demonstrated that the result is in agreement with the previous DNS data (Pirozzoli *et al.* 2008). Moreover, the linear scaling in the viscous sublayer and the logarithmic scaling in the overlap region (Smits & Dussauge 2006) are also plotted, and the present result is consistent with them. Further, the density-scaled Reynolds-stress components are shown in figure 2(*b*) and agree well

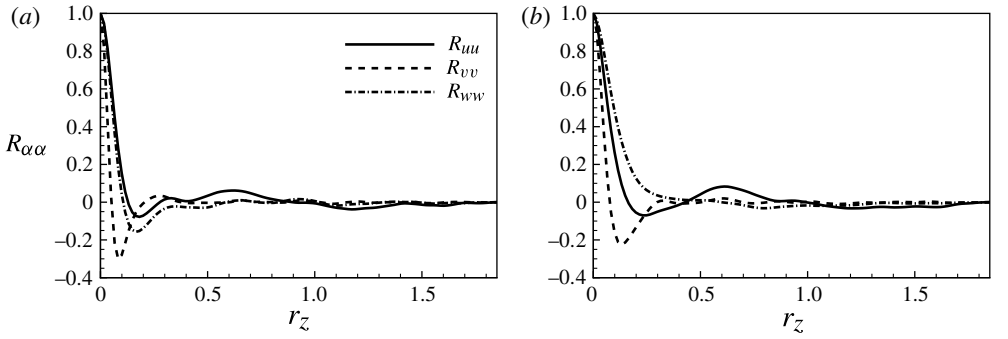

FIGURE 1. Distributions of the two-point correlations of the velocity components in the spanwise direction at (*a*) $y^+ = 4$, and (*b*) $y^+ = 65$.

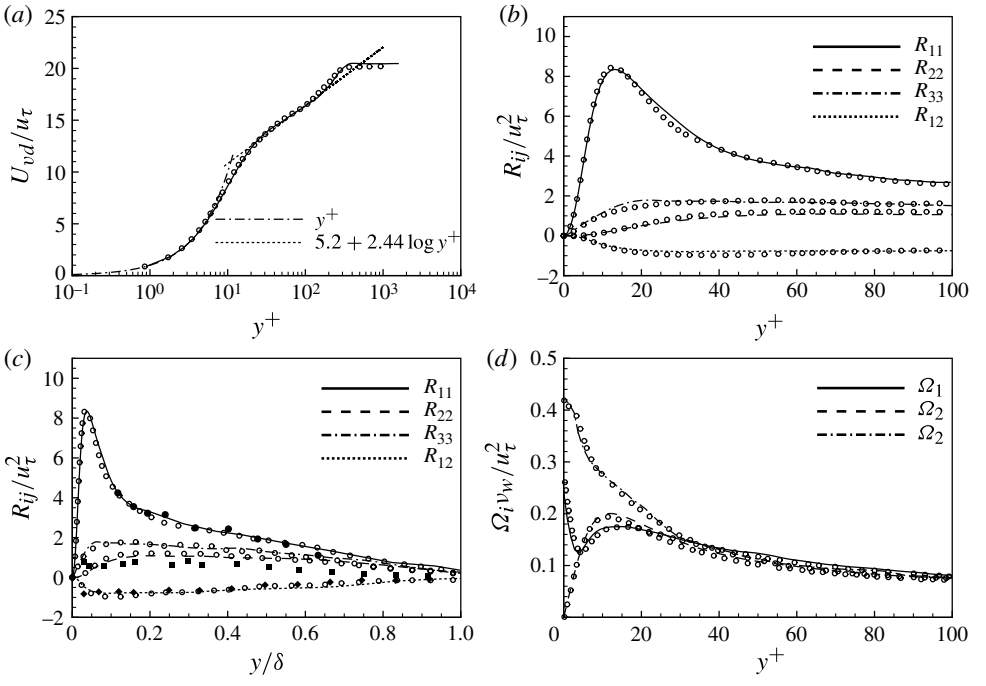

FIGURE 2. Comparisons of the calculated results with previous data. (*a*) The van Driest transformed mean streamwise velocity $U_{vd} = \int_0^{\tilde{u}} (\bar{\rho}/\bar{\rho}_w)^{1/2}\, \mathrm{d}\tilde{u}$ with linear scaling and logarithmic scaling lines (Smits & Dussauge 2006). (*b*) The density-scaled Reynolds stress components $R_{ij} = (\bar{\rho}/\bar{\rho}_w)\widetilde{u_i'' u_j''}$ in inner scaling, where the tilde means $\tilde{f} = \overline{\rho f}/\bar{\rho}$ with a decomposition $f = \tilde{f} + f''$. (*c*) R_{ij} in outer scaling with experimental data (Eléna & Lacharme 1988). (*d*) The r.m.s. vorticity components $\Omega_i = (\overline{\omega_i'^2})^{1/2}$ at $x/\delta_0 = 25$. Open symbols denote the previous DNS data (Pirozzoli *et al.* 2008) and solid symbols denote experimental data at $Ma = 2.32$ and $Re_\theta = 4700$ (Eléna & Lacharme 1988).

with the DNS data (Pirozzoli *et al.* 2008). To further assess the global behaviour of the boundary layer, the Reynolds stresses of experimental data of a supersonic boundary

layer (Eléna & Lacharme 1988) are also given in figure 2(*c*) to validate the quality of the present simulation. In addition, the distributions of the r.m.s. vorticity components are shown in figure 2(*d*). The spanwise vorticity fluctuation is obviously larger than either the streamwise or the wall-normal fluctuation in the near-wall region, consistent with the findings of Klewicki & Panton (1997). It is also seen that the calculated results agree well with those obtained by Pirozzoli *et al.* (2008). Essentially, we have carefully examined the physical model and numerical approach used in this study, and have verified that the calculated results are reliable.

The present code is equipped with a multi-block domain decomposition feature to facilitate parallel processing in a distributed computing environment. At the selected flow condition, a fully developed turbulent state is reached from $x/\delta_0 = 15$. In order to study the statistical properties of the turbulent boundary layer, we used 800 flow samples (equal intervals in time) over approximately 40 non-dimensional time units (δ_0/a_∞). The samples are collected in a small portion of the boundary layer where the momentum thickness Reynolds number Re_θ varies between 1340 and 1370. Because of the small variation of Re_θ, the growth of the boundary layer is negligible and all statistical properties are regarded to be functions only of the wall-normal coordinate (Elsinga & Marusic 2010*a*; Pirozzoli *et al.* 2010*b*). The frictional Reynolds number is determined to be $Re_\tau = 330$. We do in fact recognize the slight differences in the statistics in the streamwise direction due to the small variation of Re_θ; nevertheless, we feel that the results obtained will be reliable and helpful in the analysis of the statistical properties.

Based on the mean velocity profile in figure 2(*a*), the boundary layer is then classified into four regions by means of the standard terminology: viscous sublayer ($0 < y^+ < 7$), buffer layer ($7 < y^+ < 40$), logarithmic layer ($40 < y^+ < 140$) and wake region ($140 < y^+ < 300$). The sublayer and buffer layer are usually referred to as the 'inner layer' and the logarithmic layer and wake region as the 'outer layer' (Pirozzoli *et al.* 2008).

We have assessed the appropriateness of the spatial resolution used in this study and have also observed that statistical quantities of the invariants of the velocity gradient tensor vary sharply in the proximity of the wall. To obtain meaningful statistical results, we have calculated the invariants using 800 flow samples. Based on numerical examinations, we can trust the results in the proximity of the wall. The results will be shown from $y^+ > 2.6$, which corresponds to the fourth grid-node in the wall-normal direction, or from $y^+ = 1$ in the logarithmic scaling.

3. Invariants and local flow topology

3.1. *Definitions of the invariants*

The eigenvalues Λ_i of the velocity gradient tensor $\boldsymbol{A}$ with components $A_{ij} = \partial u_i/\partial x_j$ are obtained as solutions of the characteristic equation

$$\Lambda_i^3 + P\Lambda_i^2 + Q\Lambda_i + R = 0, \tag{3.1}$$

where P, Q and R are the first, second and third invariants of $\boldsymbol{A}$, defined by

$$P = -\mathrm{tr}(\boldsymbol{A}) = -S_{ii} = -\theta, \tag{3.2a}$$

$$Q = \tfrac{1}{2}([\mathrm{tr}(\boldsymbol{A})]^2 - \mathrm{tr}(\boldsymbol{A}^2)) = \tfrac{1}{2}(P^2 - S_{ij}S_{ji} - W_{ij}W_{ji}), \tag{3.2b}$$

$$R = -\det(\boldsymbol{A}) = \tfrac{1}{3}(-P^3 + 3PQ - S_{ij}S_{jk}S_{ki} - 3W_{ij}W_{jk}S_{ki}), \tag{3.2c}$$

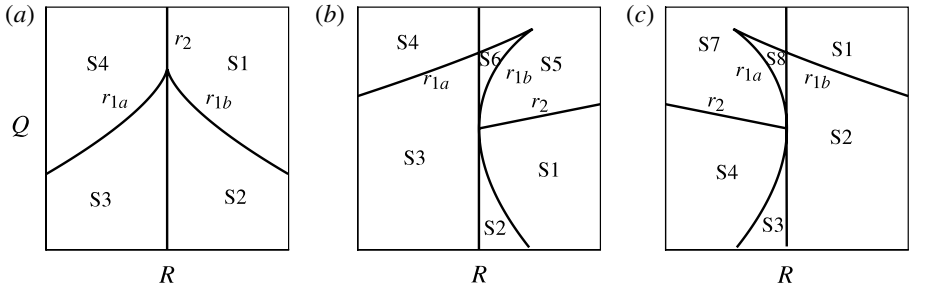

FIGURE 3. The topological classification in the Q–R plane for (*a*) $P = 0$, (*b*) $P > 0$, and (*c*) $P < 0$. The topologies and corresponding acronyms are listed in table 1.

where $S_{ij} = (A_{ij} + A_{ji})/2$ is the symmetric strain-rate tensor; $W_{ij} = (A_{ij} - A_{ji})/2$ is the skew-symmetric rotation-rate tensor. The invariants of S_{ij} and W_{ij} are then given by

$$P_{\boldsymbol{S}} = P = -S_{ii}, \quad Q_{\boldsymbol{S}} = \tfrac{1}{2}(P_{\boldsymbol{S}}^2 - S_{ij}S_{ji}), \quad R_{\boldsymbol{S}} = \tfrac{1}{3}(-P_{\boldsymbol{S}}^3 + 3P_{\boldsymbol{S}}Q_{\boldsymbol{S}} - S_{ij}S_{jk}S_{ki}), \tag{3.3}$$

$$P_{\boldsymbol{W}} = 0, \quad Q_{\boldsymbol{W}} = -\tfrac{1}{2}W_{ij}W_{ji}, \quad R_{\boldsymbol{W}} = 0. \tag{3.4}$$

Thus, we can obtain

$$Q = Q_{\boldsymbol{S}} + Q_{\boldsymbol{W}}, \quad R = R_{\boldsymbol{S}} - W_{ij}W_{jk}S_{ki} = R_{\boldsymbol{S}} - \tfrac{1}{4}\omega_i S_{ij}\omega_j. \tag{3.5}$$

Note that $Q_{\boldsymbol{W}}$ is positive definite and $Q_{\boldsymbol{S}}$ is negative definite.

3.2. *Topology in P–Q–R space*

The flow topology of turbulent flow can be analysed in P–Q–R space using critical point terminology (Perry & Chong 1987; Chong *et al.* 1990). The surface $\Delta = 0$ divides the space into two regions, where Δ is the discriminant of (3.1) and is defined by

$$\Delta = \tfrac{27}{4}R^2 + (P^3 - \tfrac{9}{2}PQ)R + (Q^3 - \tfrac{1}{4}P^2Q^2). \tag{3.6}$$

In the region $\Delta > 0$, $\boldsymbol{A}$ has one real and two complex-conjugate eigenvalues, while in the region $\Delta < 0$, $\boldsymbol{A}$ has three real, distinct eigenvalues. The surface $\Delta = 0$ can be split into two surfaces r_{1a} and r_{1b}, which osculate to form a cusp and are given by

$$\tfrac{1}{3}P(Q - \tfrac{2}{9}P^2) - \tfrac{2}{27}(-3Q + P^2)^{3/2} - R = 0, \tag{3.7a}$$

$$\tfrac{1}{3}P(Q - \tfrac{2}{9}P^2) + \tfrac{2}{27}(-3Q + P^2)^{3/2} - R = 0. \tag{3.7b}$$

Further, in the region $\Delta > 0$, $\boldsymbol{A}$ has purely imaginary eigenvalues on the surface r_2, which is described by

$$PQ - R = 0. \tag{3.8}$$

Moreover, the flow pattern is two-dimensional on the surface $R = 0$ (Chong *et al.* 1990). Thus, the surfaces r_{1a}, r_{1b}, r_2 and $R = 0$ divide P–Q–R space into different regions, and each of these regions corresponds to a topology.

It is convenient to investigate the flow topology in the Q–R plane for a selected value of P (Suman & Girimaji 2010). Then, the surfaces r_{1a}, r_{1b}, r_2 and $R = 0$ appear simply as the corresponding curves, which divide the Q–R plane into various regions. For $P = 0$, the curve r_2 is coincident with the Q axis, and the curves r_{1a} and r_{1b} are symmetric to each other with respect to the Q axis. Then four topologies are identified, which are schematically exhibited in figure 3(*a*). For $P \neq 0$, as shown in figure 3(*b,c*),

Sector	Acronym	Description
S1	UFC	Unstable focus/compressing
S2	UN/S/S	Unstable node/saddle/saddle
S3	SN/S/S	Stable node/saddle/saddle
S4	SFS	Stable focus/stretching
S5	SFC	Stable focus/compressing
S6	SN/SN/SN	Stable node/stable node/stable node
S7	UFS	Unstable focus/stretching
S8	UN/UN/UN	Unstable node/unstable node/unstable node

TABLE 1. Summary of the acronyms of various flow topologies in P–Q–R space.

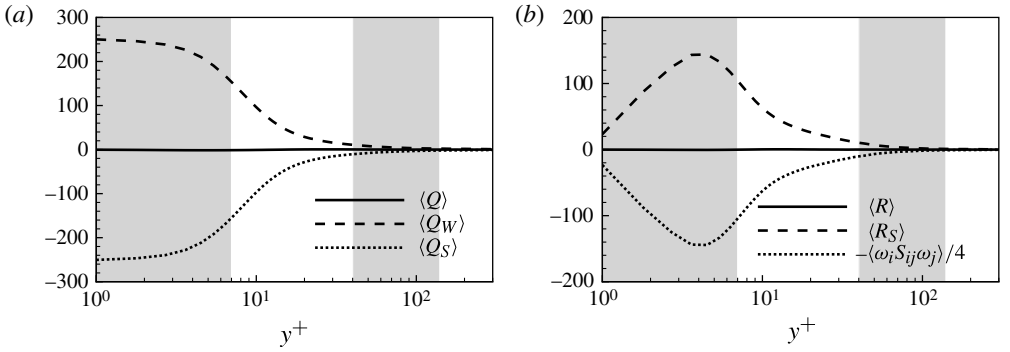

FIGURE 4. Transverse distributions of the mean invariants and the relevant quantity. The shaded and white areas differentiate the viscous sublayer, buffer layer, logarithmic layer and wake region.

r_2 intersects with the curve r_{1b} for $P > 0$ and with the curve r_{1a} for $P < 0$ at $Q = 0$ and $R = 0$. Consequently, the Q–R plane is divided into six regions for $P > 0$ and $P < 0$, respectively. The topologies and corresponding acronyms are listed in table 1.

4. Results and discussion

4.1. *Statistical properties of the invariants*

4.1.1. *Mean invariants*

We first investigate the properties of some invariants in the viscous sublayer, buffer layer, logarithmic layer and wake region of the boundary layer. Note that, to reveal the effect of the mean shear on the statistical properties, the invariants are calculated using the velocity gradient without subtracting the gradient of the mean velocity components. The distributions of the mean invariants along the wall-normal direction are shown in figure 4. It is seen from figure 4(*a*) that $\langle Q_{\boldsymbol{W}}\rangle$, which represents the enstrophy physically, attains a large value in the sublayer and then decreases with the increase in y^+. $\langle Q_{\boldsymbol{S}}\rangle$ measures the local dissipation per unit viscosity, and its change is opposite to $\langle Q_{\boldsymbol{W}}\rangle$ with $\langle Q\rangle = \langle Q_{\boldsymbol{W}}\rangle + \langle Q_{\boldsymbol{S}}\rangle$ approaching zero across the boundary layer. Moreover, $\omega_i S_{ij}\omega_j$ represents the enstrophy production rate and $R_{\boldsymbol{S}}$ the dissipation production rate occurring in the dissipation evolution (Tsinober 2000; Chevillard *et al.* 2008). As shown in figure 4(*b*), $\langle\omega_i S_{ij}\omega_j\rangle/4$ increases to a peak in the sublayer and

then decreases with y^+. $\langle R_S \rangle$ exhibits an approximately similar profile with $\langle \omega_i S_{ij} \omega_j \rangle/4$ and $\langle R \rangle = \langle R_S \rangle - \langle \omega_i S_{ij} \omega_j \rangle/4$ is nearly zero in the boundary layer.

From the distributions of the invariants in figure 4, it is observed that on average the viscous sublayer is a relatively high-enstrophy, high-dissipation region with large enstrophy production and large dissipation production. This statistical feature confirms the finding that the high-strain/high-enstrophy regions are the most important ones for the strain and vorticity production processes based on an experimental investigation of Lagrangian correlations of small-scale turbulence (Guala *et al.* 2007). Further, figure 4(*b*) shows that $\langle \omega_i S_{ij} \omega_j \rangle$ is positive in the boundary layer, which is consistent with the fact that enstrophy production (vortex stretching) prevails over enstrophy destruction (vortex compression) (Taylor 1938). Moreover, the positive $\langle R_S \rangle$ is related to the self-amplification of velocity derivatives (Galanti & Tsinober 2000).

4.1.2. *Joint p.d.f. of the invariants*

The statistical characteristics of the invariants are further studied in terms of their joint probability density function (p.d.f.). Owing to the complexity of three-dimensional joint p.d.f.s in P–Q–R space, it is convenient to exhibit the flow topology in the Q–R plane for selected values of P (Suman & Girimaji 2009, 2010). Here, we choose three typical values of P, i.e. -3, 0 and 3, to analyse the joint p.d.f.s in the Q–R plane as shown in figure 5, where the invariants P, Q and R are normalized by $\langle Q_W \rangle^{1/2}$, $\langle Q_W \rangle$ and $\langle Q_W \rangle^{3/2}$, respectively (Ooi *et al.* 1999). It is seen that the contours of the joint p.d.f.s for $P = 0$ exhibit self-similar teardrop shapes around the origin, which have widely been observed for turbulent flows numerically (Soria *et al.* 1994; Blackburn *et al.* 1996; Chong *et al.* 1998; Ooi *et al.* 1999; Pirozzoli & Grasso 2004; Suman & Girimaji 2010) and experimentally (Gulitski *et al.* 2007; Tsinober 2009; Elsinga & Marusic 2010*a*). In the viscous sublayer, where the mean shear is high, the shapes of the contours are very similar to the stratified homogeneous sheared turbulence with high shear (Diamessis & Nomura 2000; Nomura & Diamessis 2000).

Further, the contours of the joint p.d.f.s for $P = 3$ also illustrate the self-similar shapes in figure 5. Compared with the p.d.f.s for $P = 0$, it is observed that the shapes become more symmetric; more points tend to be stable topologies (S3, S4 and S5) while fewer points tend to be unstable topologies (S1 and S2). It means that the locally compressed region is favourable to the stable topologies. On the contrary, the contours of the joint p.d.f.s for $P = -3$ exhibit more skewed shapes with respect to those for $P = 0$, indicating that the locally expanding region is favourable to the unstable topologies.

The turbulent flow behaviour is analysed based on the local flow topology in the Q–R plane. As $Q = Q_W + Q_S$ and $R = R_S - \omega_i S_{ij} \omega_j/4$, we can understand that Q represents the competition between enstrophy and dissipation, and R the competition between enstrophy production and dissipation production. The enstrophy production in S4:SFS is usually positive and large (Tsinober 2000). The more symmetric shapes of the joint p.d.f.s for $P = 3$ reflect that the enstrophy production is less prevalent in locally compressed regions, and the more skewed shapes of the joint p.d.f.s for $P = -3$ indicate that the enstrophy production is more prevalent in locally expanding flows. These statistical features can be explained by means of the enstrophy transport equation (Kida & Orszag 1990). As the mean flow is compressed (i.e. $\langle \theta \rangle < 0$, where $\theta = \partial u_i/\partial x_i$), the dilatation term $-\langle \theta \omega_i \omega_i \rangle/2$ acts to enhance the enstrophy. In a statistical steady state, the enstrophy production term $\langle \omega_i S_{ij} \omega_j \rangle$ must be decreased to

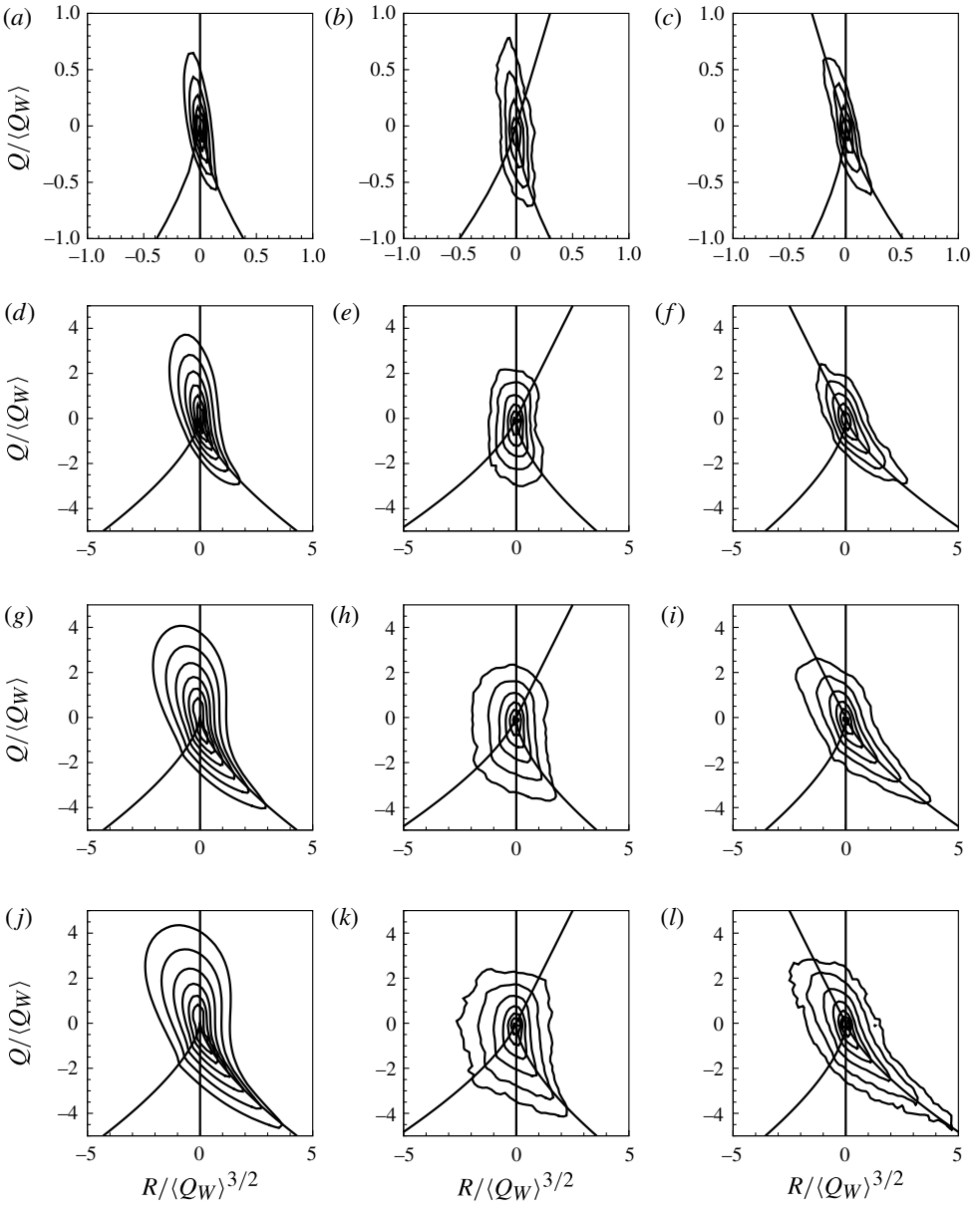

FIGURE 5. Joint p.d.f.s of Q and R on a logarithmic scale in the viscous sublayer (*a–c*), buffer layer (*d–f*), logarithmic layer (*g–i*) and wake region (*j–l*). (*a,d,g,j*) $P = 0$, (*b,e,h,k*) $P = 3$, and (*c,f,i,l*) $P = -3$. The outer contour level is -3 and the inner contour level is 0. The separation between successive contour levels is 0.5. The same contour levels are used in figures for the joint p.d.f.s.

maintain the enstrophy in equilibrium (Guala *et al.* 2007). On the other hand, as the mean flow is expanding ($\langle\theta\rangle > 0$), the enstrophy production term $\langle\omega_i S_{ij}\omega_j\rangle$ must be increased to maintain the enstrophy in equilibrium.

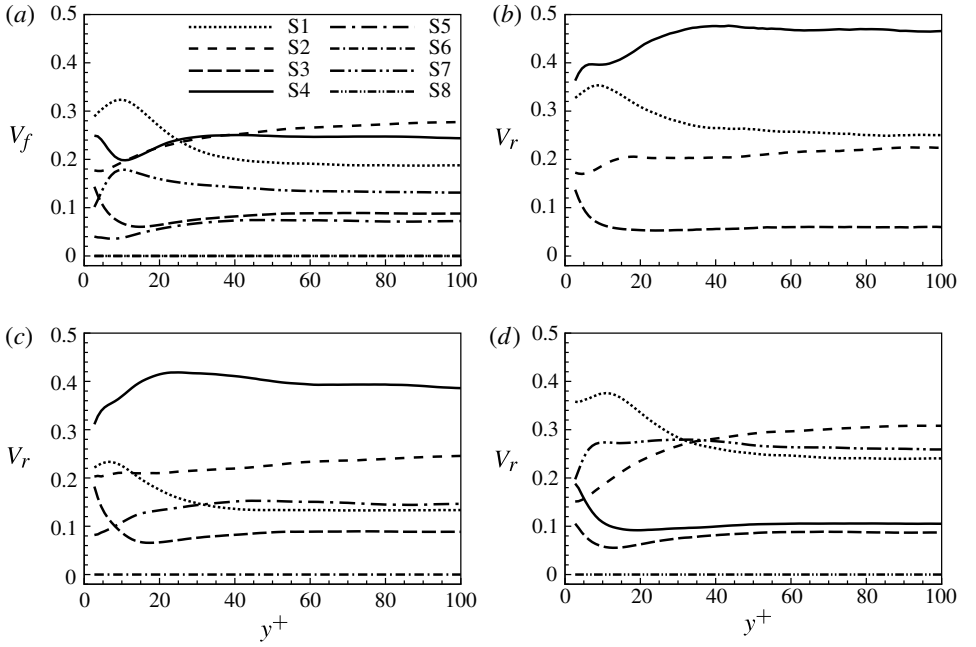

FIGURE 6. Occurrence probabilities of the various topologies in the boundary layer: (*a*) constructed from the whole region, (*b*) constructed from the region $|P| < 0.001$, (*c*) constructed from the region $P > 0$, (*d*) constructed from the region $P < 0$.

4.2. *Flow topology and the relevant feature*

In order to quantitatively characterize the statistical properties in *P*–*Q*–*R* space, the occurrence probabilities of the flow topologies (S1–S8) are studied. As the mesh is uniformly distributed in the streamwise and spanwise directions, the occurrence probability is equivalent to the volume fraction. To clarify the compressibility effect, the occurrence probabilities are analysed for the $P > 0$ (or compressed) and $P < 0$ (or expanding) regions, respectively. For comparison, the relative volume fractions of the flow topologies in the 'incompressible' region with P around zero are discussed. Moreover, the geometric characteristics of the focal topologies are further investigated.

4.2.1. *Occurrence probability of the topology*

The occurrence probabilities of the various topologies are shown in figure 6(*a*). It is seen that the probabilities change markedly along y^+ in the inner layer where the mean shear is high, and attain nearly constant values in the outer layer where the mean shear becomes low. The most probable topology is S1:UFC in the inner layer and is S2:UN/S/S in the outer layer. Furthermore, S4:SFS is the second most probable topology in the boundary layer. Compared with the compressible additional topologies, S7:UFS is more likely to occur than S5:SFC, and the occurrence probabilities of S6:SN/SN/SN and S8:UN/UN/UN are nearly zero due to the weak compressibility. Moreover, it is observed from figure 6(*a*) that the unstable topologies (S1, S2 and S7) prevail over the stable topologies (S3, S4 and S5). This statistical property can also be elucidated from figure 7(*a*). It is seen that the mean flow tends to be expanding, while expansion means outward flow and is defined to as unstable.

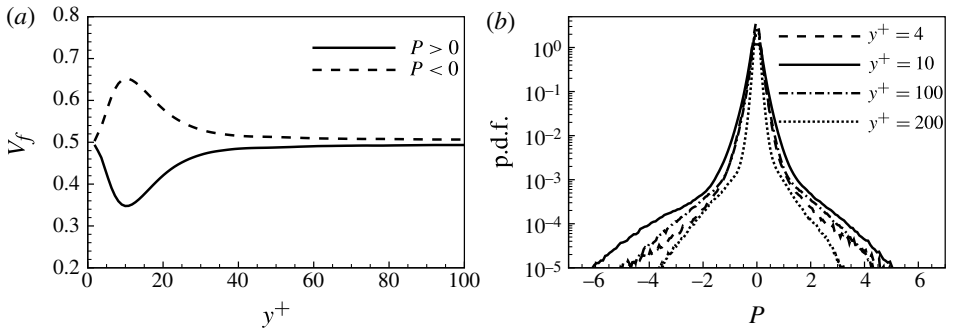

FIGURE 7. (*a*) Transverse distributions of the volume fraction of $P > 0$ and $P < 0$. (*b*) Probability density function of the dilatation at four wall-normal locations.

The occurrence probabilities of the topologies in the 'incompressible' region are obtained using conditional statistics upon zero dilatation or $|P| < \epsilon$, where ϵ is a threshold value. To obtain meaningful results in the 'incompressible' region, we have chosen $\epsilon = 0.001$ based on our examinations. It must be understood that, even though the selection of ϵ may be somewhat arbitrary, the relative statistical results for $|P| < \epsilon$ are nearly unchanged as long as the sample number is sufficiently large. As shown in figure 6(*b*), S4 is most likely to occur and S1 is the second most probable topology. In the outer layer, the probabilities are nearly unchanged along y^+ and are consistent with those for incompressible turbulence (Buxton & Ganapathisubramani 2010) and for compressible isotropic turbulence conditional upon zero dilatation (Suman & Girimaji 2010). The probabilities also reveal that focal topologies (S1 and S4) prevail over non-focal topologies (Pirozzoli & Grasso 2004).

From figure 6(*a,b*), we can see that compressibility obviously influences the flow topology, even though the turbulent Mach number is less than 0.3 and some flow statistical quantities are similar to the incompressible cases (e.g. Spina, Smits & Robinson 1994; Pirozzoli *et al.* 2008; Ringuette *et al.* 2008; Duan, Beekman & Martin 2011). The most probable topology changes from S4 for incompressible flow to S1 in the inner layer and to S2 in the outer layer for compressible flow. Thus, the effect of compressibility restrains the occurrence of S4 and results in more unstable flow.

As illustrated in figures 3 and 5, the topological features of compressible turbulence depend on the first invariant P. To distinguish the effect of $P > 0$ (or $\theta < 0$) and $P < 0$ (or $\theta > 0$), we consider the occurrence probabilities of the topologies constructed from the regions $P > 0$ (compressed) and $P < 0$ (expanding), respectively. For $P > 0$, figure 6(*c*) shows that S4 remains the most probable topology in the boundary layer, and S1 becomes less frequent compared with the 'incompressible' region. Analogously, figure 6(*d*) shows the occurrence probabilities for $P < 0$. Compared with the results for $P > 0$, the probability of S4 is decreased significantly and the probability of S2 is increased. Moreover, S1 prevails over the other topologies in the inner layer and S2 over the other ones in the outer layer. It is also seen that the unstable topologies (S1, S2 and S7) are more likely to occur than the stable topologies (S3, S4 and S5) for $P < 0$. In addition, for both $P > 0$ and $P < 0$, the occurrence probabilities of S6 and S8 nearly vanish. Therefore, the locally compressed region tends to restrain the occurrence of S1:UFC (unstable focus/compressing) and the locally expanding region to restrain the occurrence of S4:SFS (stable focus/stretching).

To compare with the compressed and expanding effects, figure 7(*a*) shows the transverse distributions of the volume fraction for the regions $P > 0$ and $P < 0$. It is seen that the compressed and expanding regions are approximately equivalent for $y^+ > 40$, while the expansion is more frequent than the compression around $y^+ = 10$. This statistical feature is related to the density variation close to the wall. Moreover, the occurrence probabilities of the various topologies in figure 6(*a*) can be obtained by combining the results of $P > 0$ and $P < 0$. Consequently, the probabilities in the inner layer in figure 6(*a*) are similar to those in figure 6(*d*). The p.d.f.s of P are further examined and exhibited in figure 7(*b*). It is seen that the tail at $y^+ = 10$ is more skewed to the $P < 0$ domain, consistent with the behaviour of the volume fraction in figure 7(*a*).

4.2.2. *Geometric characteristics of the focal topologies*

The topological classification in the plane of invariants provides additional geometric information on the vortical structures. Using critical point theory, Chong *et al.* (1990) defined a vortex core to be the region where $\Delta > 0$. Consequently, the focal topologies (i.e. S1, S4, S5 and S7) correspond to various vortical structures, and are described as follows: S1:UFC corresponds to a vortex undergoing radial expansion and axial compression, S4:SFS a vortex undergoing radial contraction and axial stretching, S5:SFC a vortex contracting in both radial and axial directions, and S7:UFS a vortex expanding in both radial and axial directions (Suman & Girimaji 2010).

From the preceding analysis of the results in figure 6, it is clear that the vortical structures are most likely to undergo radial expansion and axial compression in the inner layer and to undergo radial contraction and axial stretching in the outer layer. Moreover, the incompressible region is most likely occupied by the vortical structures subjected to radial contraction and axial stretching. In the locally compressed region, the occurrence probability of radial expanding and axial compressed vortical structures is decreased significantly. In the locally expanding region, the occurrence probability of radial contracting and axial stretching vortical structures is decreased considerably, and therefore the vortical structures in the outer layer are more likely to undergo expansion in both radial and axial directions.

Further, we use the Q criterion (Hunt, Wray & Moin 1988) to identify the vortical structures. Figure 8(*a*) shows the instantaneous iso-surface of Q for the regions with focal topologies in the outer layer. It is seen that the S4:SFS regions are compact and occupy most of the focal volume, consistent with the occurrence probabilities in figure 6(*a*). To clearly exhibit the relevant vortical structures, as shown in figure 8(*b*), the S4:SFS and S7:UFS regions resemble tube-like structures and are in general elongated. The S7:UFS structures are mainly observed in the regions where the S4:SFS structure bends or in the regions where two S4:SFS structures join. It means that the compressibility obviously influences the geometric characteristics of the vortical structures, even though the compressible turbulent boundary layers apparently exhibit vortical structures similar to those of the incompressible case (e.g. Smith & Smits 1995; Ganapathisubramani *et al.* 2006; Ringuette *et al.* 2008; Pirozzoli *et al.* 2008; Elsinga & Marusic 2010*a*). Moreover, as shown in figure 8(*c*), the S1:UFC and S5:SFC regions resemble blob-like structures and are stretched into ramp-shaped structures by the mean shear and small-scale turbulent motions (Girimaji & Pope 1990; Yang & Pullin 2011). Thus we can understand why the stretching focal regions tend to form tube-like structures and the compressed focal regions tend to form blob-like structures.

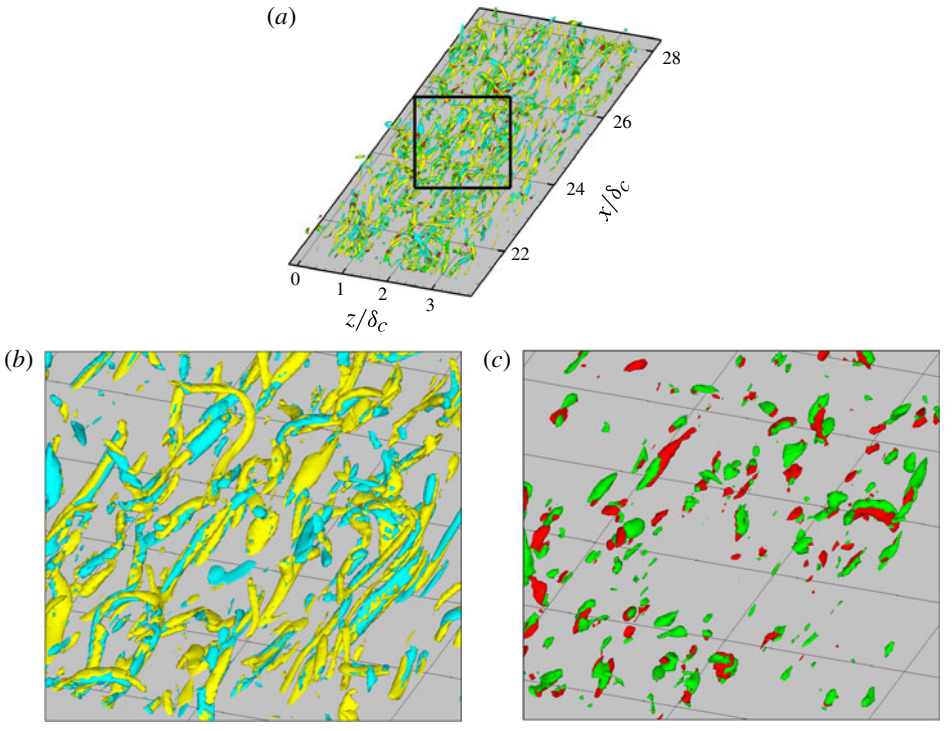

FIGURE 8. Iso-surface of $Q = 10$ used to visualize focal structures in the outer layer. In (*a*), the red iso-surface represents flow regions with S1:UFC topology, the yellow iso-surface S4:SFS topology, the blue iso-surface S5:SFC topology, and the green iso-surface S7:UFS topology. For a clear illustration, the S4:SFS and S7:UFS structures are redrawn in (*b*), and the S1:UFC and S5:SFC structures in (*c*).

4.3. *Invariants of the topology*

We further study the conditional average invariants of the various topologies. To distinguish the effects of compressibility, the conditional statistical results are constructed from the regions $P > 0$ and $P < 0$, respectively. For comparison, the invariants in the 'incompressible' region determined by the approach in § 4.2.1 are also analysed. All the conditional average invariants are normalized by the corresponding mean values in figure 4. As the occurrence probabilities of S6 and S8 are small, we only consider the topologies S1, S2, S3, S4, S5 and S7. Moreover, recall that $\langle R_{\boldsymbol{S}}\rangle = 0$ and $\langle \omega_i S_{ij} \omega_j\rangle = 0$ at the wall, and $\langle Q_{\boldsymbol{W}}\rangle$ and $\langle Q_{\boldsymbol{S}}\rangle$ approach zero in the wake region. Thus, the characteristics of the invariants are mainly investigated in $0 < y^+ < 100$.

4.3.1. $Q_{\boldsymbol{S}}$ *and* $Q_{\boldsymbol{W}}$

Figure 9 shows the conditional average dissipation of the topologies constructed from different regions relevant to the compressibility. From figure 9(*a*), for the whole region consisting of the 'incompressible', compressed and expanding regions, the dissipation of the unstable node/saddle/saddle (S2) topology is the largest one, indicating that the dissipation is closely related to the unstable strain-dominated region. Moreover, S1, S4 and S7 are responsible for a major proportion of dissipation, while S5 only accounts for a small proportion of dissipation. Thus, both the focal and

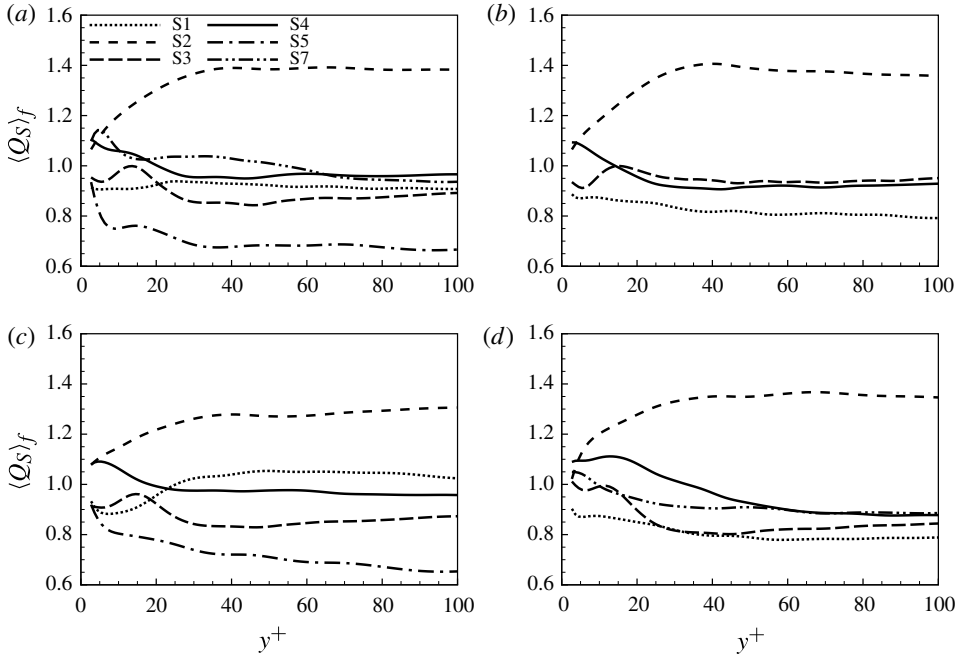

FIGURE 9. Conditional average dissipation of the various topologies in the boundary layer: (*a*) constructed from the whole region, (*b*) constructed from the region $|P| < 0.001$, (*c*) constructed from the region $P > 0$, and (*d*) constructed from the region $P < 0$.

non-focal topologies play an important role in the dissipation in compressible turbulent boundary layers, consistent with compressible isotropic turbulence (Pirozzoli & Grasso 2004). As shown in figure 9(*b*) for the 'incompressible' region, S2 remains the most important topology for the dissipation. Compared with the results in figure 9(*a,b*), the dissipation of S1 and S4 increases slightly and the dissipation of S3 decreases. Further, as exhibited in figure 9(*c,d*) for the compressed and expanding regions, the dissipation of S2 remains higher than that of the other topologies. The dissipation of S1 is increased in the locally compressed region and the dissipation of S4 is increased in the locally expanding region. Moreover, the change of the dissipation versus y^+ also reflects the influence of the mean shear on the statistical properties of the topologies.

The conditional average enstrophy of the various topologies is shown in figure 10. From figure 10(*a*), the enstrophy of S7 is the highest one for the whole region. Moreover, the enstrophy of S4 and S5 is also high and the enstrophy of S1 is moderate, while the enstrophy of S2 and S3 is low. Thus, we obtain that the enstrophy mainly comes from the focal topologies (S1, S4, S5 and S7). For the 'incompressible' region, figure 10(*b*) shows that S4 is responsible for the largest proportion of the enstrophy, which is obviously different from that in figure 10(*a*). For the compressed and expanding regions, figure 10(*c,d*) indicates that the enstrophy of S1 is decreased in the locally compressed region and the enstrophy of S4 is significantly decreased in the locally expanding region. Physically, the enstrophy reflects the rotation strength of the fluid element. As the mean shear is high in the near-wall region, the rotation energy mostly originates from the high mean shear, and therefore the values of the conditional

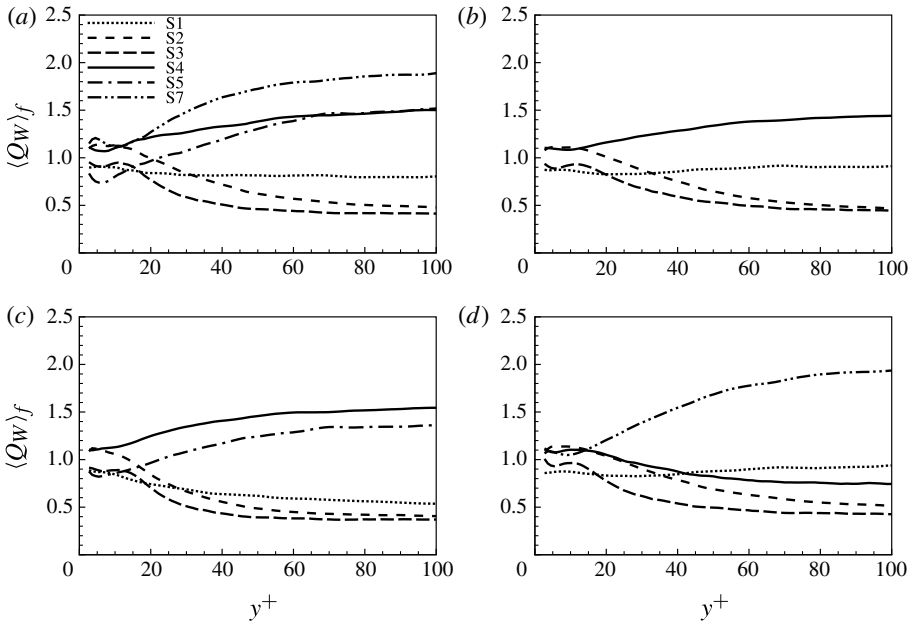

FIGURE 10. Conditional average enstrophy of the various topologies in the boundary layer. For other details see figure 9.

average enstrophy for all topologies are reasonably close to 1 in figure 10. This is also the reason why $\langle Q_s \rangle_f$ is close to 1 for all the topologies in figure 9.

4.3.2. *R_S and $\omega_i S_{ij} \omega_j$*

The conditional average productions of enstrophy and dissipation are further investigated. Figure 11 shows the conditional average dissipation production rates of the various topologies. It is seen that S2 is the most important topology for the dissipation production for all the regions. As shown in figure 11(*a*), the dissipation production rates of the non-focal topologies (S2 and S3) are larger than those of the focal topologies (S1, S4, S5 and S7) in the inner layer, and the dissipation production rates of S1, S4 and S7 are similar to each other in the outer layer. It is also noticed that the average dissipation production of S5 is negative in the inner layer and approaches zero in the outer layer. Thus, we learn that the focal topologies is not as important for the strain production as the non-focal topologies. Compared with figure 11(*b–d*), the compressed region tends to increase the dissipation production of S1, and the expanding region tends to increase the dissipation production of S4 in the inner layer.

Figure 12 shows the conditional average enstrophy production rates of the various topologies. The enstrophy production in figure 12(*a*) mainly comes from S2 in the inner layer and from S7 in the outer layer. In addition, S4 also contributes a major proportion of the enstrophy production and S1 accounts for a small proportion of the enstrophy production in the outer layer. Furthermore, the enstrophy production of S5 is negative in the boundary layer, indicating that vortex compressing prevails over vortex stretching. As shown in figure 12(*b*) for the 'incompressible' region, S2 remains the most important topology for the enstrophy production in the inner layer and S4 is responsible for a large proportion of the enstrophy production in the

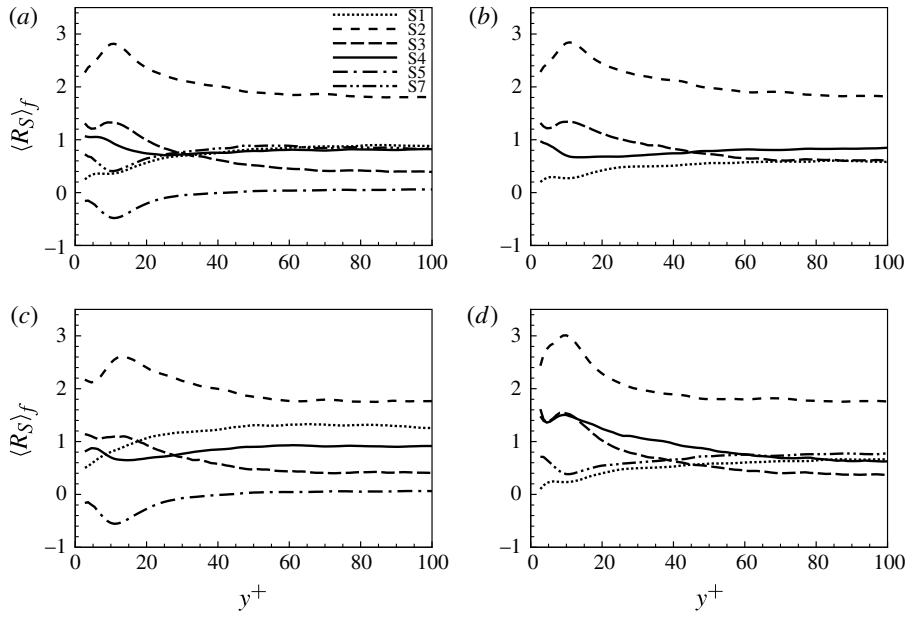

FIGURE 11. Conditional average dissipation production of the various topologies in the boundary layer. For other details see figure 9.

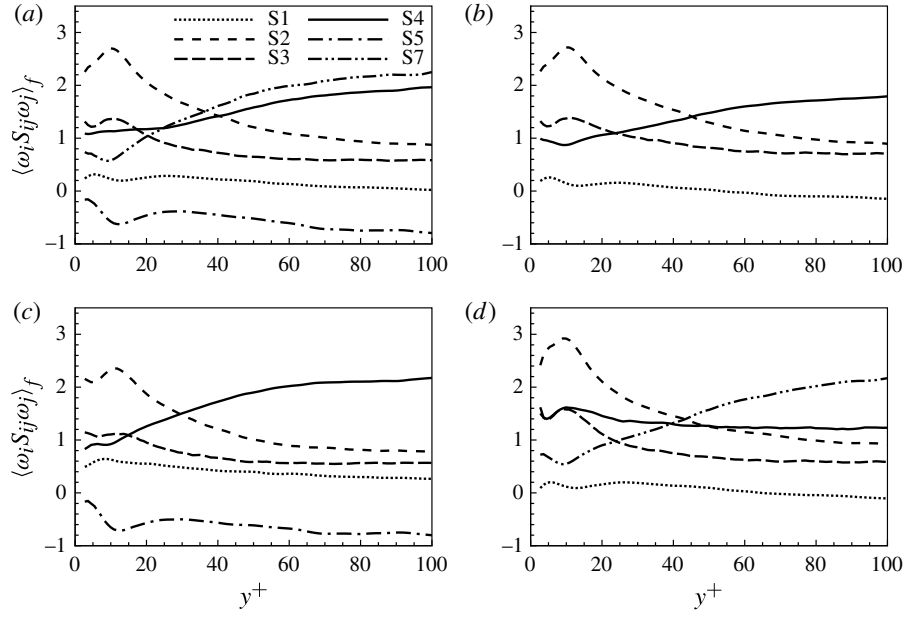

FIGURE 12. Conditional average enstrophy production of the various topologies in the boundary layer. For other details see figure 9.

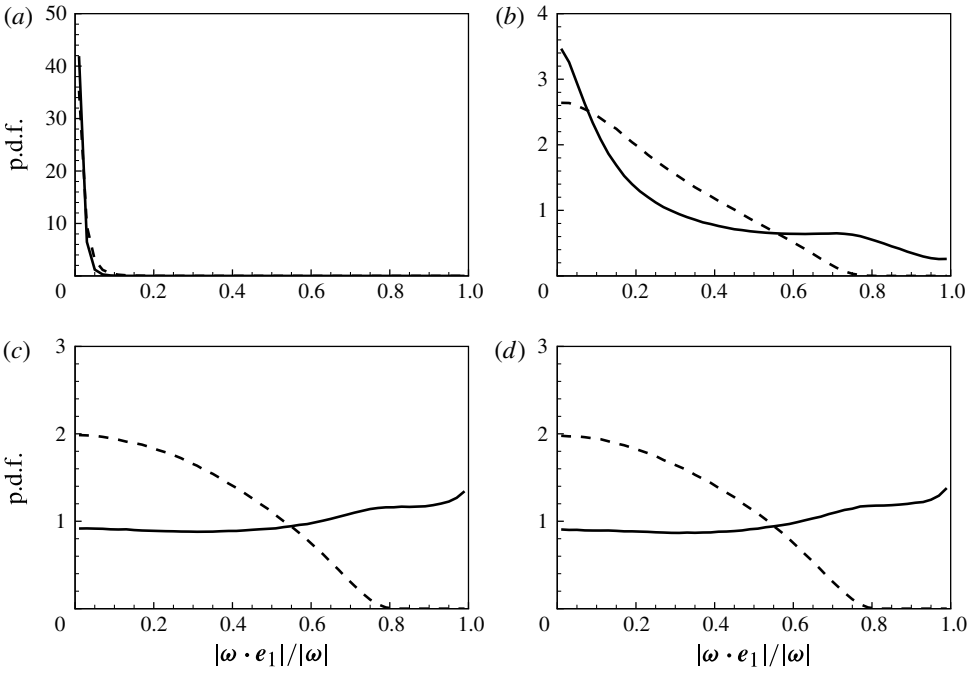

FIGURE 13. Probability density function of the cosine of the alignment angle between $\boldsymbol{\omega}$ and $\boldsymbol{e}_1$ in the (*a*) viscous sublayer, (*b*) buffer layer, (*c*) logarithmic layer, and (*d*) wake region. The solid lines represent the p.d.f.s constructed from the enstrophy-producing region ($\omega_i S_{ij}\omega_j > 0$) and the dashed lines the p.d.f.s constructed from the enstrophy-destroying region ($\omega_i S_{ij}\omega_j < 0$).

outer layer. The values of the conditional average enstrophy production rates in the outer layer agree quantitatively with the results in incompressible isotropic turbulence (Buxton & Ganapathisubramani 2010). To gain insight into the compressibility effect on the enstrophy production, the enstrophy production rates for the compressed and expanding regions are shown in figure 12(*c,d*). It is observed that the compressed region tends to increase the enstrophy production of S1 and the expanding region tends to increase the enstrophy production of S4 in the inner layer.

From figures 11 and 12, it is also obtained that the dissipation production is mainly related to the strain-dominated region (S2) in the inner and outer layers, while the enstrophy production is related to S2 in the inner layer and to S7 in the outer layer. These statistical properties further confirm the findings reported by Tsinober (2000): the enstrophy production requires strain and its interaction with vorticity, but the dissipation production is in some sense less dependent on vorticity, even though it is impossible without vorticity.

Furthermore, the enstrophy production is also related to the alignments between the vorticity vector ($\boldsymbol{\omega}$) and the eigenvectors $\boldsymbol{e}_i$, which are shown in figures 13–15, respectively. In the inner layer, $\boldsymbol{\omega}$ is preferentially perpendicular to the most extensive strain-rate eigenvector $\boldsymbol{e}_1$ and the compressive strain-rate eigenvector $\boldsymbol{e}_3$, and aligns with the intermediate strain-rate eigenvector $\boldsymbol{e}_2$ for the enstrophy production ($\omega_i S_{ij}\omega_j > 0$) and the enstrophy destruction ($\omega_i S_{ij}\omega_j < 0$). In the outer layer, the alignment p.d.f.s exhibit the difference for $\omega_i S_{ij}\omega_j > 0$ and $\omega_i S_{ij}\omega_j < 0$. From figure 13(*c,d*), a slight

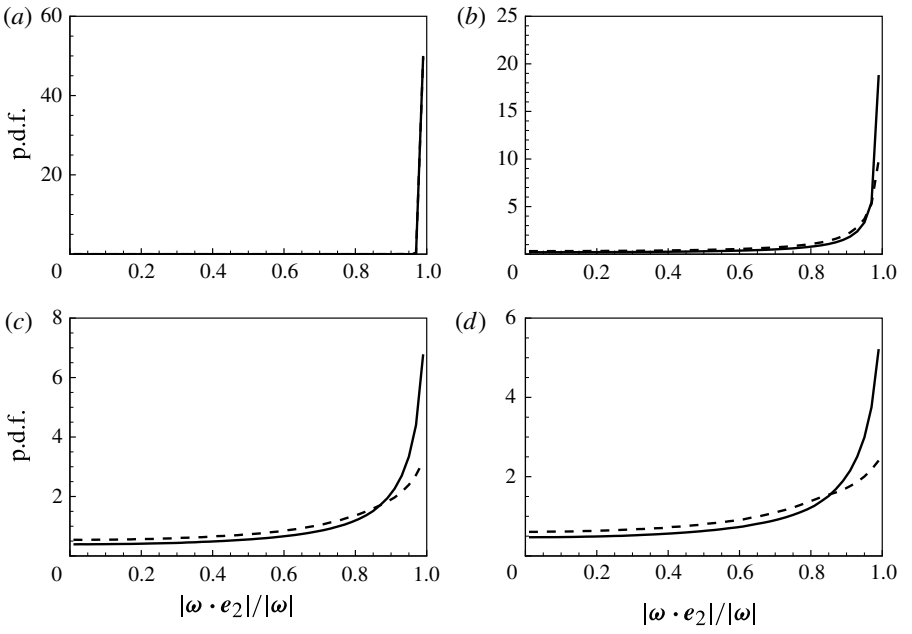

FIGURE 14. Probability density function of the cosine of the alignment angle between $\boldsymbol{\omega}$ and $\boldsymbol{e}_2$ in the (*a*) viscous sublayer, (*b*) buffer layer, (*c*) logarithmic layer, and (*d*) wake region. For other details see figure 13.

tendency for $\boldsymbol{\omega}$ to align with $\boldsymbol{e}_1$ is observed for $\omega_i S_{ij}\omega_j > 0$, and the perpendicular tendency between $\boldsymbol{\omega}$ and $\boldsymbol{e}_1$ is obtained for $\omega_i S_{ij}\omega_j < 0$, essentially consistent with the previous finding (Buxton & Ganapathisubramani 2010). From figure 14(*c,d*), $\boldsymbol{\omega}$ tends to align with $\boldsymbol{e}_2$ for $\omega_i S_{ij}\omega_j > 0$ and $\omega_i S_{ij}\omega_j < 0$. The tendency for $\boldsymbol{\omega}$ to align with $\boldsymbol{e}_2$ is exaggerated in the enstrophy-producing region as opposed to the enstrophy-destroying region. Further, from figure 15(*c,d*), $\boldsymbol{\omega}$ tends to be perpendicular to $\boldsymbol{e}_3$ for the enstrophy production and prefers to be inclined at an angle of approximately 45° with respect to $\boldsymbol{e}_3$ (the maximum of the p.d.f. occurring at $|\boldsymbol{\omega}\cdot\boldsymbol{e}_3|/|\boldsymbol{\omega}| \approx 0.7$) for the enstrophy destruction due to the effect of the mean shear. Moreover, we have observed that the predominant enstrophy production region occurs around 3/4 of the fluid flow domain in the wake region, which is essentially similar to around 2/3 for incompressible turbulence (Tsinober 2009). Thus, it is plausible that the perpendicular tendency between $\boldsymbol{\omega}$ and $\boldsymbol{e}_3$ is still predominant in the wake region.

Physically, the enstrophy production is essentially a nonlinear process of the interaction between strain and vorticity (Tsinober 2009). In the inner layer, the enstrophy production is strongly depressed in regions dominated by enstrophy as compared to those dominated by strain (Tsinober, Ortenberg & Shtillman 1999). Consequently, the conditional average enstrophy production rate of S2 is high in figure 12. In the outer layer, as the mean shear is low, the statistical properties are similar to the quasi-isotropic turbulence (Galanti & Tsinober 2000). The largest contribution to the enstrophy production originates from the regions in which the vorticity vector is aligned to a predominantly stretching eigenvector (Tsinober, Shtilman & Vaisburd 1997; Tsinober 1998; Buxton & Ganapathisubramani 2010).

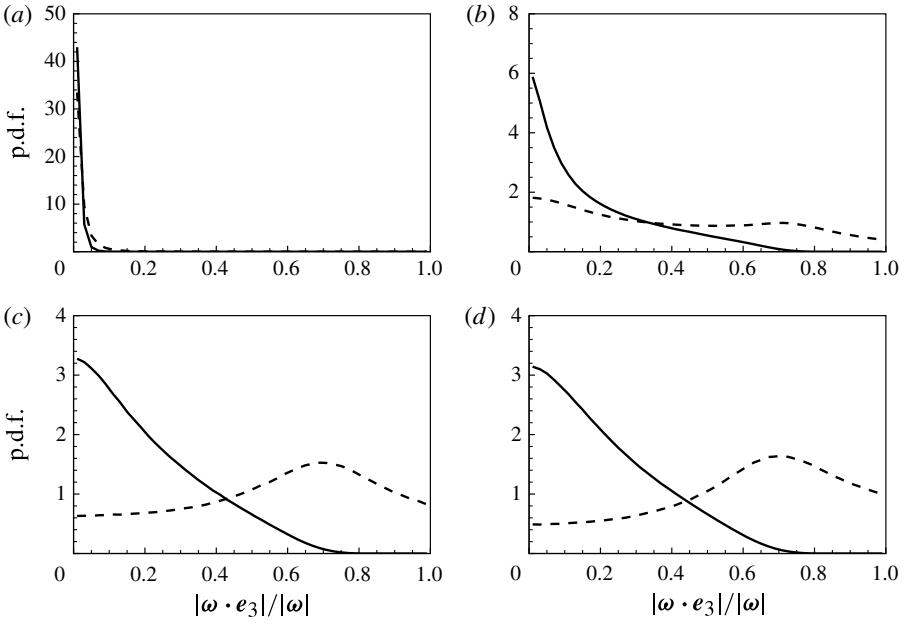

FIGURE 15. Probability density function of the cosine of the alignment angle between $\boldsymbol{\omega}$ and $\boldsymbol{e}_3$ in the (*a*) viscous sublayer, (*b*) buffer layer, (*c*) logarithmic layer, and (*d*) wake region. For other details see figure 13.

5. Concluding remarks

The flow topologies and statistical properties of compressible turbulent boundary layers at Mach 2 are studied in terms of the detailed analysis of the invariants of the velocity gradient tensor. The main conclusions are briefly summarized as follows.

The statistical characteristics of the invariants in the viscous sublayer, buffer layer, logarithmic layer and wake region of the boundary layer are analysed. It is revealed that the viscous sublayer is a relatively high-enstrophy, high-dissipation region, and the largest enstrophy production and largest dissipation production occur at approximately $y^+ = 4$. For a given value of the first invariant, the joint p.d.f.s of the second and third invariants exhibit self-similar shapes in the boundary layer. Moreover, it is found that the enstrophy production for the positive dilatation is usually larger than that for the negative dilatation.

The occurrence probabilities of the various topologies are analysed for the 'incompressible', compressed and expanding regions, respectively. We find that the compressible turbulent boundary layer is probably dominated by the vortical structures undergoing radial expansion and axial compression in the inner layer and the unstable strain-dominated structures in the outer layer. The locally compressed region tends to be more stable and the locally expanding region tends to be more dissipative. Further, it is revealed that the compressibility is mainly related to the radial expansion and axial compression, as well as the radial contracting and axial stretching vortical structures.

Based on the analysis of geometric characteristics of the focal topologies, it is observed that the stretching focal regions tend to form tube-like structures and the compressing focal regions tend to form blob-like structures. It is also found that the

most probable vortical structures in the outer layer undergo radial contraction and axial stretching for the whole region, and undergo expansion in both radial and axial directions for the locally expanding region.

The conditional average dissipation, enstrophy, dissipation production and enstrophy production of the various topologies are also investigated. It is found that the dissipation and dissipation production mainly originate from UN/S/S topology. The enstrophy relies mainly on UFS topology, and the enstrophy production depends on UN/S/S topology in the inner layer and on UFS topology in the outer layer. Compared with the 'incompressible' region, in the locally compressed region, the average enstrophy of UFC is decreased, while the average dissipation, dissipation production and enstrophy production of UFC are increased. In the locally expanding region, the average enstrophy of SFS is decreased, while the average dissipation, dissipation production and enstrophy production of SFS are increased.

Acknowledgements

The authors are very grateful to Professor S. Pirozzoli for valuable discussion and Professor C. W. Shu for providing the two-dimensional WENO code. This work was supported by the National Natural Science Foundation of China (Grants 11132010 and 11072236) and the 111 Project (Grant B07033).

REFERENCES

ABE, H., ANTONIA, R. A. & KAWAMURA, H. 2009 Correlation between small-scale velocity and scalar fluctuations in a turbulent channel flow. *J. Fluid Mech.* **627**, 1–32.

ADAMS, N. A. 1998 Direct numerical simulation of turbulent compression ramp flow. *Theor. Comput. Fluid Dyn.* **12**, 109–129.

ANDREOPOULOS, Y. & HONKAN, A. 2001 An experimental study of the dissipative and vortical motion in turbulent boundary layers. *J. Fluid Mech.* **439**, 131–163.

BERMEJO-MORENO, I., PULLIN, D. I. & HORIUTI, K. 2009 Geometry of enstrophy and dissipation, resolution effects and proximity issues in turbulence. *J. Fluid Mech.* **620**, 121–166.

BIJLARD, M. J., OLIEMANS, R. V. A., PORTELA, L. M. & OOMS, G. 2010 Direct numerical simulation analysis of local flow topology in a particle-laden turbulent channel flow. *J. Fluid Mech.* **653**, 35–56.

BLACKBURN, H. M., MANSOUR, N. & CANTWELL, B. J. 1996 Topology of fine-scale motions in turbulent channel flow. *J. Fluid Mech.* **301**, 269–292.

VAN DER BOS, F., TAO, B., MENEVEAU, C. & KATZ, J. 2002 Effects of small-scale turbulent motions on the filtered velocity gradient tensor as deduced from holographic particle image velocimetry measurements. *Phys. Fluids* **14** (7), 2456–2474.

BUXTON, O. R. H. & GANAPATHISUBRAMANI, B. 2010 Amplification of enstrophy in the far field of an axisymmetric turbulent jet. *J. Fluid Mech.* **651**, 483–502.

CANTWELL, B. J. 1992 Exact solution of a restricted Euler equation for the velocity gradient tensor. *Phys. Fluids* A **4** (4), 782–793.

CHACIN, J. M. & CANTWELL, B. J. 2000 Dynamics of a low Reynolds number turbulent boundary layer. *J. Fluid Mech.* **404**, 87–115.

CHACÍN, J. M., CANTWELL, B. J. & KLINE, S. J. 1996 Study of turbulent boundary layer structure using the invariants of the velocity gradient tensor. *Exp. Therm. Fluid Sci.* **13**, 308–317.

CHERTKOV, M., PUMIR, A. & SHRAIMAN, B. I. 1999 Lagrangian tetrad dynamics and the phenomenology of turbulence. *Phys. Fluids* **11** (8), 2394–2410.

CHEVILLARD, L., MENEVEAU, C., BIFERALE, L. & TOSCHI, F. 2008 Modeling the pressure Hessian and viscous Laplacian in turbulence: comparisons with direct numerical simulation and implications on velocity gradient dynamics. *Phys. Fluids* **20**, 101504.

CHONG, M. S., PERRY, A. E. & CANTWELL, B. J. 1990 A general classification of three-dimensional flow fields. *Phys. Fluids* A **2** (5), 765–777.

CHONG, M. S., SORIA, J., PERRY, A. E., CHACIN, J., CANTWELL, B. J. & NA, Y. 1998 Turbulence structures of wall-bounded shear flows found using DNS data. *J. Fluid Mech.* **357**, 225–247.

DIAMESSIS, P. J. & NOMURA, K. K. 2000 Interaction of vorticity, rate-of-strain, and scalar gradient in stratified homogeneous sheared turbulence. *Phys. Fluids* **12** (5), 1166–1188.

DUAN, L., BEEKMAN, I. & MARTIN, M. P. 2011 Direct numerical simulation of hypersonic turbulent boundary layers. Part 3. Effect of Mach number. *J. Fluid Mech.* **672**, 245–267.

ELÉNA, M. & LACHARME, J. 1988 Experimental study of a supersonic turbulent boundary layer using a laser Doppler anemometer. *J. Méc. Théor. Appl.* **7**, 175–190.

ELSINGA, G. E., ADRIAN, R. J., VAN OUDHEUSDEN, B. W. & SCARANO, F. 2010 Three-dimensional vortex organization in a high-Reynolds-number supersonic turbulent boundary layer. *J. Fluid Mech.* **644**, 35–60.

ELSINGA, G. E. & MARUSIC, I. 2010*a* Evolution and lifetimes of flow topology in a turbulent boundary layer. *Phys. Fluids* **22**, 015102.

ELSINGA, G. E. & MARUSIC, I. 2010*b* Universal aspects of small-scale motions in turbulence. *J. Fluid Mech.* **662**, 514–539.

GALANTI, B. & TSINOBER, A. 2000 Self-amplification of the field of velocity derivatives in quasi-isotropic turbulence. *Phys. Fluids* **12**, 3097–3099.

GANAPATHISUBRAMANI, B., CLEMENS, N. T. & DOLLING, D. S. 2006 Large-scale motions in a supersonic turbulent boundary layer. *J. Fluid Mech.* **556**, 271–282.

GIRIMAJI, S. S. & POPE, S. B. 1990 Material-element deformation in isotropic turbulence. *J. Fluid Mech.* **220**, 427–458.

GUALA, M., LIBERZON, A., TSINOBER, A. & KINZELBACH, W. 2007 An experimental investigation on Lagrangian correlations of small-scale turbulence at low Reynolds number. *J. Fluid Mech.* **574**, 405–427.

GUALTIERI, P. & MENEVEAU, C. 2010 Direct numerical simulations of turbulence subjected to a straining and destraining cycle. *Phys. Fluids* **22**, 065104.

GUARINI, S. E., MOSER, R. D., SHARIFF, K. & WRAY, A. 2000 Direct numerical simulation of a supersonic boundary layer at Mach 2.5. *J. Fluid Mech.* **414**, 1–33.

GULITSKI, G., KHOLMYANSKY, M., KINZELBACH, W., LÜTHI, B., TSINOBER, A. & YORISH, Y. 2007 Velocity and temperature derivatives in high-Reynolds-number turbulent flows in the atmospheric surface layer. Part 1. Facilities, methods and some general results. *J. Fluid Mech.* **589**, 57–81.

HUNT, J. C. R., WRAY, A. A. & MOIN, P. 1988 Eddies, streams, and convergence zones in turbulent flows. In *Rep. CTR-S88, Center for Turbulence Research*. Stanford University.

JEONG, J. & HUSSAIN, F. 1995 On the identification of a vortex. *J. Fluid Mech.* **285**, 69–94.

JIANG, G. S. & SHU, C. W. 1996 Efficient implementation of weighted ENO schemes. *J. Comput. Phys.* **126**, 202–228.

KHASHEHCHI, M., ELSINGA, G. E., OOI, A., SORIA, J. & MARUSIC, I. 2010 Studying invariants of the velocity gradient tensor of a round turbulent jet across the turbulent/nonturbulent interface using Tomo-PIV. In *Laser Techniques Applied to Fluid Mechanics, 15th International Symposium*., Lisbon, Portugal.

KIDA, S. & ORSZAG, S. A. 1990 Enstrophy budget in decaying compressible turbulence. *J. Sci. Comput.* **5** (1), 1–34.

KLEWICKI, J. C. 1997 Self-sustaining traits of near-wall motions underlying boundary layer stress transport. In *Self-Sustaining Mechanisms of Wall Turbulence* (ed. R. L. Panton), pp. 135–166. Computational Mechanics Publications.

LEE, K., GIRIMAJI, S. S. & KERIMO, J. 2009 Effect of compressibility on turbulent velocity gradients and small-scale structure. *J. Turbul.* **10** (9), 1–18.

LI, Q. & COLEMAN, G. N. 2003 DNS of an oblique shock wave impinging upon a turbulent boundary layer. In *Direct and Large-Eddy Simulation V*, pp. 387–396. Kluwer.

LI, Y., CHEVILLARD, L., EYINK, G. & MENEVEAU, C. 2009 Matrix exponential-based closures for the turbulent subgrid-scale stress tensor. *Phys. Rev.* E **79**, 016305.

LI, Y. & MENEVEAU, C. 2005 Origin of non-Gaussian statistics in hydrodynamic turbulence. *Phys. Rev. Lett.* **95**, 164502.

LI, Y. & MENEVEAU, C. 2006 Intermittency trends and Lagrangian evolution of non-Gaussian statistics in turbulent flow and scalar transport. *J. Fluid Mech.* **558**, 133–142.

LÜTHI, B., HOLZNER, M. & TSINOBER, A. 2009 Expanding the *Q–R* space to three dimensions. *J. Fluid Mech.* **641**, 497–507.

MAEKAWA, H., HIYAMA, T. & MATSUO, Y. 1999 Study of the geometry of flow patterns in compressible isotropic turbulence. *JSME Intl J.* **42**, 336–343.

MENEVEAU, C. 2011 Lagrangian dynamics and models of the velocity gradient tensor in turbulent flows. *Annu. Rev. Fluid Mech.* **43**, 219–245.

NOMURA, K. K. & DIAMESSIS, P. J. 2000 The interaction of vorticity and rate-of-strain in homogeneous sheared turbulence. *Phys. Fluids* **12** (4), 846–864.

NOMURA, K. K. & POST, G. K. 1998 The structure and dynamics of vorticity and rate of strain in incompressible homogeneous turbulence. *J. Fluid Mech.* **377**, 65–97.

OOI, A., MARTÍN, J., SORIA, J. & CHONG, M. S. 1999 A study of the evolution and characteristics of the invariants of the velocity-gradient tensor in isotropic turbulence. *J. Fluid Mech.* **381**, 141–174.

PERRY, A. E. & CHONG, M. S. 1987 A description of eddying motions and flow patterns using critical point concepts. *Annu. Rev. Fluid Mech.* **19**, 125–155.

PERRY, A. E. & CHONG, M. S. 1994 Topology of flow patterns in vortex motions and turbulence. *Appl. Sci. Res* **53**, 357–374.

PIROZZOLI, S., BERNARDINI, M. & GRASSO, F. 2008 Characterization of coherent vortical structures in a supersonic turbulent boundary layer. *J. Fluid Mech.* **613**, 205–231.

PIROZZOLI, S., BERNARDINI, M. & GRASSO, F. 2010*a* Direct numerical simulation of transonic shock/boundary layer interaction under conditions of incipient separation. *J. Fluid Mech.* **657**, 361–393.

PIROZZOLI, S., BERNARDINI, M. & GRASSO, F. 2010*b* On the dynamical relevance of coherent vortical structures in turbulent boundary layers. *J. Fluid Mech.* **648**, 325–349.

PIROZZOLI, S. & GRASSO, F. 2004 Direct numerical simulations of isotropic compressible turbulence: influence of compressibility on dynamics and structures. *Phys. Fluids* **16** (12), 4386–4407.

PIROZZOLI, S., GRASSO, F. & GATSKI, T. B. 2004 Direct numerical simulation and analysis of a spatially evolving supersonic turbulent boundary layer at $M = 2.25$. *Phys. Fluids* **16** (3), 530–545.

RINGUETTE, M. J., WU, M. & MARTIN, M. P. 2008 Coherent structures in direct numerical simulation of turbulent boundary layers at Mach 3. *J. Fluid Mech.* **594**, 59–69.

SANDHAM, N. D., YAO, Y. F. & LAWAL, A. A. 2003 Large-eddy simulation of transonic turbulent flow over a bump. *Intl J. Heat Fluid Flow* **24**, 584–595.

SHU, C. W. & OSHER, S. 1988 Efficient implementation of essentially non-oscillatory shock-capturing schemes. *J. Comput. Phys.* **77**, 439–471.

DA SILVA, C. B. & PEREIRA, J. C. F. 2008 Invariants of the velocity-gradient, rate-of-strain, and rate-of-rotation tensors across the turbulent/nonturbulent interface in jets. *Phys. Fluids* **20**, 055101.

SMITH, M. W. & SMITS, A. J. 1995 Visualization of the structures of supersonic turbulent boundary layers. *Exp. Fluids* **18**, 288–302.

SMITS, A. J. & DUSSAUGE, J. P. 2006 *Turbulent Shear Layers in Supersonic Flow*. American Institute of Physics.

SORIA, J. & CANTWELL, B. J. 1994 Topological visualisation of focal structures in free shear flows. *Appl. Sci. Res.* **53**, 375–386.

SORIA, J., SONDERGAARD, R., CANTWELL, B. J., CHONG, M. S. & PERRY, A. E. 1994 A study of the fine-scale motions of incompressible time-developing mixing layers. *Phys. Fluids* **6** (2), 871–884.

SPINA, E. F., SMITS, A. J. & ROBINSON, S. K. 1994 The physics of supersonic turbulent boundary layers. *Annu. Rev. Fluid Mech.* **26**, 287–319.

SUMAN, S. & GIRIMAJI, S. S. 2009 Homogenized Euler equation: a model for compressible velocity gradient dynamics. *J. Fluid Mech.* **620**, 177–194.

SUMAN, S. & GIRIMAJI, S. S. 2010 Velocity gradient invariants and local flow field topology in compressible turbulence. *J. Turbul.* **11** (2), 1–24.

TAYLOR, G. I. 1938 Production and dissipation of vorticity in a turbulent fluid. *Proc. R. Soc. Lond.* A **164**, 15–23.

TSINOBER, A. 1998 Is concentrated vorticity that important? *Eur. J. Mech.* B **17** (4), 421–449.

TSINOBER, A. 2000 Vortex stretching versus production of strain/dissipation. In *Turbulence Structure and Vortex Dynamics*, pp. 164–191. Cambridge University Press.

TSINOBER, A. 2009 *An Informal Conceptual Introduction to Turbulence*, second edition. Springer.

TSINOBER, A., ORTENBERG, M. & SHTILLMAN, L. 1999 On depression of nonlinearity in turbulence. *Phys. Fluids* **11** (8), 2291–2297.

TSINOBER, A., SHTILMAN, L. & VAISBURD, H. 1997 A study of properties of vortex stretching and enstrophy generation in numerical and laboratory turbulence. *Fluid Dyn. Res.* **21**, 477–494.

WALLACE, J. M. 2009 Twenty years of experimental and direct numerical simulation access to the velocity gradient tensor: What have we learned about turbulence? *Phys. Fluids* **21**, 021301.

WANG, B. C., BERGSTROM, D. J., YIN, J. & YEE, E. 2006 Turbulence topologies predicted using large eddy simulations. *J. Turbul.* **7** (34), 1–28.

WANG, L. & LU, X.-Y. 2011 Statistical analysis of coherent vortical structures in a supersonic turbulent boundary layer. *Chin. Phys. Lett.* **28**, 034703.

WHITE, F. M. 1974 *Viscous Fluid Flow*. McGraw-Hill.

YANG, Y. & PULLIN, D. I. 2011 Geometric study of Lagrangian and Eulerian structures in turbulent channel flow. *J. Fluid Mech.* **674**, 67–92.